

Velocity-strengthening friction significantly affects interfacial dynamics, strength and dissipation

Yohai Bar-Sinai¹, Robert Spatschek², Efim A. Brener^{1,3} and Eran Bouchbinder¹

¹*Chemical Physics Department, Weizmann Institute of Science, Rehovot 76100, Israel*

²*Max-Planck-Institut für Eisenforschung GmbH, D-40237 Düsseldorf, Germany*

³*Peter Grünberg Institut, Forschungszentrum Jülich, D-52425 Jülich, Germany*

Frictional interfaces are abundant in natural and man-made systems and their dynamics still pose challenges of fundamental and technological importance. A recent extensive compilation of multiple-source experimental data has revealed that velocity-strengthening friction, where the steady-state frictional resistance increases with sliding velocity over some range, is a generic feature of such interfaces. Moreover, velocity-strengthening friction has very recently been linked to slow laboratory earthquakes and stick-slip motion. Here we elucidate the importance of velocity-strengthening friction by theoretically studying three variants of a realistic rate-and-state friction model. All variants feature identical logarithmic velocity-weakening friction at small sliding velocities, but differ in their higher velocity behaviors. By quantifying energy partition (e.g. radiation and dissipation), the selection of interfacial rupture fronts and rupture arrest, we show that the presence or absence of velocity-strengthening friction can significantly affect the global interfacial resistance and the total energy released during frictional instabilities (“event magnitude”). Furthermore, we show that different forms of velocity-strengthening friction (e.g. logarithmic vs. linear) may result in events of similar magnitude, yet with dramatically different dissipation and radiation rates. This happens because the events are mediated by interfacial rupture fronts with vastly different propagation velocities, where stronger velocity-strengthening friction promotes slower rupture. These theoretical results may have significant implications on our understanding of frictional dynamics.

I. INTRODUCTION

Frictional interfaces are abundant in biological (e.g. adherent cells and cell locomotion), engineering (e.g. micro-electro-mechanical devices) and geophysical (e.g. Earthquake faults) systems around us, and are of fundamental and practical importance. Consequently, understanding the dynamics of dry frictional interfaces has been the focus of intense scientific activity in the last few decades [1–6]. It has been established that under steady-state sliding conditions, the frictional resistance features a non-trivial velocity dependence, and that this dependence has dramatic consequences on the dynamic response of frictional interfaces [7–12]. Specifically, it has been shown that for a broad range of materials friction is velocity-weakening – that is, the steady frictional resistance is a decreasing function of the sliding velocity – at least in the regime of low velocities, up to a few hundreds of microns per second. This feature favors various instabilities and stick-slip motion [5, 13–15].

A very recent compilation of a large set of experimental data for a broad range of materials, however, has revealed that for higher slip velocities, friction generically becomes velocity-strengthening over some range of slip velocities [16]. The existence of velocity-strengthening behavior might have significant effects on various aspects of frictional dynamics. In particular, recent laboratory experiments on fault-zone materials have documented slow slip interfacial events – an intensely debated issue – and have linked it to a crossover in the frictional response, from velocity-weakening to velocity-strengthening friction, with increasing slip velocity [12]. While the possible implications of the existence of velocity-strengthening

friction have been rather sporadically discussed in the literature [11, 12, 17–26], to the best of our knowledge a comprehensive and systematic theoretical exploration of these important issues is currently missing.

As a first step in closing this gap, we study here the effect of velocity-strengthening friction on spatiotemporal interfacial dynamics, energy dissipation and radiation, and the global interfacial strength, with a special focus on the nucleation, propagation and arrest of rupture fronts. We explore three variants of a realistic rate-and-state friction law, one which is purely velocity-weakening, one which crosses over at higher velocities to logarithmic velocity-strengthening friction, and one which crosses over to linear velocity-strengthening friction.

We show that the presence or absence of velocity-strengthening friction at relatively high slip velocities can significantly affect the global interfacial resistance (strength) and the energy released during frictional instabilities (“event magnitude”), even under quasi-static loading conditions. Different forms of velocity-strengthening friction, in our case logarithmic and linear, give rise to events of similar magnitude, yet with dramatically different dissipation and radiation rates. The difference stems from the broad range of the underlying rupture propagation velocities, where stronger velocity-strengthening friction promotes slower rupture, possibly orders of magnitude slower than elastic wave-speeds. This result is directly related to the recent experimental observations of [12]. All in all, our results show that velocity-strengthening friction should be properly quantified and incorporated into friction theory as it appears to affect many basic properties of spatially extended frictional interfaces.

II. THEORETICAL CONSIDERATIONS

The ideas to be presented below have been originally influenced by the works in [25–27] and then further developed in [16, 20, 21, 23]. The rate-and-state friction model we study has been introduced recently in [21, 23], and is reviewed here briefly. We start by considering a multi-contact interface and write the ratio A of the real contact area (the area of all contact asperities) to the nominal one, in terms of a state parameter ϕ (of time dimensions) as

$$A(\phi) = \frac{\sigma}{\sigma_H} \left[1 + b \log \left(1 + \frac{\phi}{\phi^*} \right) \right], \quad (1)$$

where σ is the normal (compressive) stress at the interface, σ_H is the material hardness, b is a dimensionless material parameter of order 10^{-2} , and ϕ^* is a short time cutoff [16, 28–30]. ϕ is usually interpreted as the interface’s effective age, and its evolution is given by

$$\partial_t \phi = 1 - \frac{\phi v}{D} g(v), \quad (2)$$

where v is the local interfacial slip velocity and D is a lengthscale related to the contact asperities geometry. $g(v) = \sqrt{1 + (v_0/v)^2}$, with an extremely small $v_0 = 1\text{nm/s}$, is a regularization function that plays no important role, and is actually omitted in all of the analytic results that follow. As we focus here on unidirectional motion, we do not distinguish between v and $|v|$.

The frictional stress τ is written as a sum of an elastic contribution, τ^{el} , and a viscous contribution τ^{vis} ,

$$\tau = \tau^{el} + \tau^{vis}. \quad (3)$$

The viscous contribution takes the form $\tau^{vis} = A(\phi) w(v)$, where at least at low velocities, the rheological part $w(v)$ corresponds to a stress-biased thermally-activated process [11, 16, 30]

$$w(v) = \frac{k_B T}{\Omega} \log \left(1 + \frac{v}{v^*} \right). \quad (4)$$

Here, k_B is Boltzmann’s constant, T is the absolute temperature, Ω is an activation volume and v^* is a velocity scale, related to a microscopic attempt rate. A higher velocity variant of Eq. (4) will be discussed below.

The elastic stress follows the evolution equation

$$\partial_t \tau^{el} = \frac{G_0}{h} A v - \tau^{el} \frac{v}{D} g(v), \quad (5)$$

where G_0 is the interfacial shear modulus and h is the effective height of the interface.

Equations (1)–(5) describe the first variant of the friction model we study below. We begin by describing its behavior under steady sliding at a velocity v_d . The steady solution of Eq. (2) is $\phi_{ss}(v) = D/v$, from which it follows that the contact area is a logarithmically decreasing function of v [1, 31, 32]. The fixed point of Eq. (5)

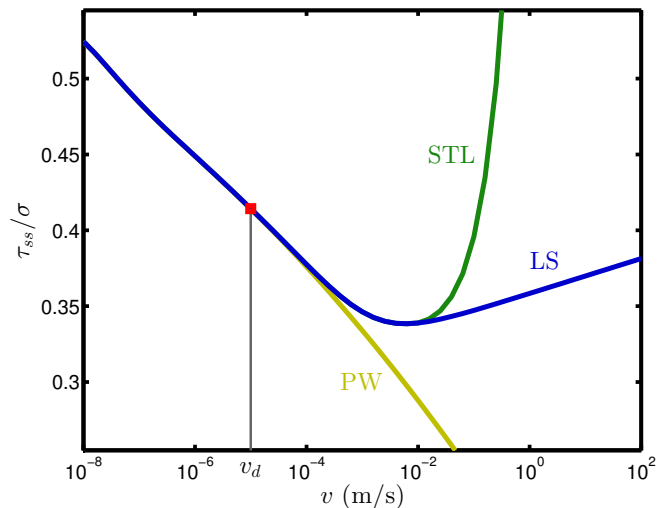


FIG. 1. The steady sliding friction coefficient τ_{ss}/σ vs. the slip velocity v for the three model variants (different colors, also marked by labels). Note that all of the curves coincide at low velocities and that the driving velocity v_d is marked.

reads $\tau_{ss}^{el}(v) = G_0 D A(\phi_{ss}(v))/h$, and hence the overall frictional resistance is given by

$$f_{ss} \equiv \frac{\tau_{ss}(v)}{\sigma} \simeq f_0 + \alpha \log \left(1 + \frac{v}{v^*} \right) + \beta \log \left(1 + \frac{D}{v\phi^*} \right), \quad (6)$$

where a higher order logarithmic term was omitted and the following definitions were used

$$\alpha \equiv \frac{k_B T}{\sigma_H \Omega}, \quad \beta \equiv \frac{G_0 D b}{h \sigma_H \Omega}, \quad f_0 \equiv \frac{\beta}{b}. \quad (7)$$

In the low velocity regime, i.e. $v \ll D/\phi^*$, f_{ss} is a logarithmic function of v , with $\partial f_{ss}/\partial \log v \approx \alpha - \beta$. Therefore, if $\alpha < \beta$ (which is quite generically the case), friction is logarithmic velocity-weakening.

Physically, friction is velocity-weakening because the real contact area is a decreasing function of the sliding velocity, and its velocity dependence is stronger than the rheological dependence of τ^{vis} . However, as discussed at length in [16, 21, 23], when $v \gtrsim D/\phi^*$ the contact area saturates, and friction becomes logarithmically velocity-strengthening. We term this model the *logarithmic velocity-strengthening* (LS) friction model. The resulting steady-state friction curve is shown in Fig. 1. In case the contact area continues to decrease indefinitely with increasing v , friction remains velocity-weakening for arbitrarily high velocities. This is formally achieved by removing the “1” in the argument of the logarithm in Eq. (1), that is, replacing Eq. (1) by

$$A(\phi) = \frac{\sigma}{\sigma_H} \left[1 + b \log \left(\frac{\phi}{\phi^*} \right) \right]. \quad (8)$$

Although this is somewhat unphysical, this choice was widely used in the literature [3, 5, 11, 33, 34], and we

term it the *pure velocity-weakening* (PW) friction model. The resulting steady-state friction curve is also shown in Fig. 1.

A third variant of the model is obtained by modifying the rheological function $w(v)$, cf. Eq. (4). As discussed extensively in [16], and to some extent in [6], the simple picture of a single barrier, linearly biased, thermally-activated process is expected to break down when asperity-level stresses become sufficiently large. When this happens, a different dissipation mechanism is expected to dominate friction. While at the moment there is no general quantitative theory for the velocity dependence of friction in this regime, it is not expected to be logarithmic, but rather to exhibit a significantly stronger dependence on the slip velocity. In this work, we consider a simple model in which the logarithmic dependence crosses over continuously (but not smoothly) to a linear viscous rheology. Explicitly, we replace Eq. (4) by

$$w(v) = \begin{cases} \frac{k_B T}{\Omega} \log\left(1 + \frac{v}{v^*}\right) & v \leq v_c \\ \frac{k_B T}{\Omega} \left[\log\left(1 + \frac{v_c}{v^*}\right) + m \left(\frac{v}{v_c} - 1\right) \right] & v > v_c \end{cases}, \quad (9)$$

where m is a dimensionless parameter. We term this model the *stronger-than-logarithmic* (STL) velocity-strengthening model. The resulting steady-state friction curve is shown in Fig. 1.

We stress that all three variants coincide in the low velocity regime, where they feature logarithmic velocity-weakening friction. At higher slip velocities, the LS variant, which is described by Eqs. (1)-(5), features a crossover to logarithmic velocity-strengthening friction. The PW variant does not feature any strengthening at all (i.e. it remains velocity-weakening), and is obtained from the LS model by using Eq. (8) instead of (1). The STL variant features linear velocity-strengthening friction, and is obtained from the LS model by using Eq. (9) instead of Eq. (4).

In order to investigate the implications of the different constitutive laws on frictional dynamics, we need to consider a spatially-extended interface under inhomogeneous sliding conditions. To this end, we consider a long elastic block of height H (in the y -direction) and length $L \gg H$ (in the x -direction), in frictional contact (at $y=0$) with a rigid substrate (i.e. no deformation of the substrate is considered), see Fig. 2. The trailing edge of the elastic block (at $x=0$) is moved at a constant velocity v_d in the positive x -direction, while the leading edge (at $x=L$) is stress-free. The block is driven quasi-statically with $v_d = 10 \mu\text{m/s}$, which is representative of typical laboratory experiments [35, 36] and generically belongs to the steady-state velocity-weakening friction branch (cf. Fig. 1). The upper edge of the elastic block (at $y=H$) experiences a constant normal stress σ , $\sigma_{yy}(x, y=H, t) = \sigma$, but no shear stress, i.e. $\sigma_{xy}(x, y=H, t) = 0$.

We focus on plane-strain deformation conditions and furthermore assume that H is smaller than the smallest lengthscale ℓ characterizing the spatial variation of vari-

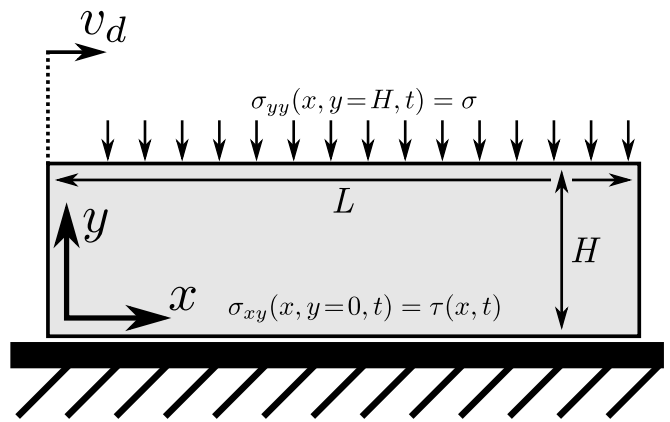


FIG. 2. A sketch of the spatially-extended frictional system. An elastic block, which is in frictional contact with a rigid substrate, is loaded by a space- and time-independent normal stress $\sigma_{yy}(x, y=H, t) = \sigma$ (H is the block's height) and driven by a velocity v_d at its trailing edge ($x=0$). The leading edge is at $x=L$. The shear stress at the interface, $\sigma_{xy}(x, y=0, t)$, equals to the frictional stress $\tau(x, t)$.

ous fields in the x -direction. Under the stated conditions, the momentum balance equation

$$\rho \partial_{tt} u_i = \partial_j \sigma_{ij}, \quad (10)$$

where u_i and σ_{ij} ($i, j = x, y$) are the components of the displacement vector and Cauchy's stress tensor, respectively, and ρ is the mass density, reduces to (see [23] for derivation)

$$\rho H \partial_{tt} u = \bar{G} H \partial_{xx} u - \tau, \quad (11)$$

$$\sigma_{yy}(x, y, t) = \sigma, \quad (12)$$

where the plane-strain Hooke's law was used. Here

$$u(x, t) \equiv \frac{1}{H} \int_0^H u_x(x, y, t) dy, \quad (13)$$

$\bar{G} = \frac{2G}{1-\nu}$ (where G is the shear modulus of the bulk and ν is Poisson's ratio) and the shear stress at $y=0$ simply equals the frictional stress, $\sigma_{xy}(x, y=0, t) = \tau(x, t)$. Note also that $v(x, t) = \partial_t u(x, t)$. Corrections to Eqs. (11)-(12) appear only to order $(H/\ell)^2$, a situation reminiscent of the shallow water approximation in fluid mechanics. Finally, note that the lateral force required to maintain the velocity boundary condition at the trailing edge, $u(x=0, t) = v_d t$, reads

$$f_d(t) = -\bar{G} H \partial_x u(x, t) \Big|_{x=0}, \quad (14)$$

and the traction-free boundary condition at the leading edge implies $\partial_x u(x=L, t) = 0$.

Equation (11), with the stated boundary conditions and with $\tau(x, t)$ corresponding to one of the three friction laws described above, has been solved numerically using a commercial differential equations solver. The model parameters for polymethyl-methacrylate (PMMA), a polymeric glass that is widely used in laboratory experiments

[35–38], were extracted from a large set of experimental data. The parameters are listed in Table I, and the procedure for obtaining them is described in [23]. The initial conditions are $u(x, t) = 0$, $v(x, t) = 0$, $\tau(x, t) = \tau^{el}(x, t) = 0$, and $\phi(x, t) = 1$ s, the latter is typical of laboratory scale experiments. The results presented here are largely insensitive to the choice of the initial value of ϕ .

\bar{G}	9.3 GPa	σ	1 MPa
G_0/h	300 MPa/ μm	b	0.075
ρ	1,200 Kg/m ³	D	0.5 μm
v^*	0.1 $\mu\text{m/s}$	D/ϕ^*	1.5 mm/s
$\frac{k_B T}{\Omega}$	27 MPa	σ_H	540 MPa
m	25	v_c	7.5 mm/s

TABLE I. Material parameters for PMMA^a.

^a Except for m and v_c , which have not been yet directly measured for this material. For such measurements in other materials, see Fig. 1 in [16].

III. RESULTS

A. Global frictional resistance

We begin by studying the macroscopic response of the system. Figure 3 shows the total frictional force exerted by the loading machine as a function of time, $f_d(t)$. It is seen that the friction force increases gradually until it experiences an abrupt drop, followed by repeated cycles of gradual increases and abrupt drops, typical of frictional systems [35, 39, 40]. The drops in the friction force, which appear as vertical lines in this figure, occur when sliding becomes unstable, and involve nucleation and propagation of rupture fronts, as will be discussed below.

Before the first drop, the friction force corresponding to the three variants is identical, as can be expected because the dynamics in this regime are slow and governed by the loading velocity v_d . In this range of velocities, the three variants coincide and consequently the first drop occurs almost exactly at the same point in time for all of the variants, suggesting that the instability mechanism is insensitive to the high velocity behavior (as predicted in [23]). However, since the instabilities are accompanied by much larger velocities, the high velocity behavior of the friction law becomes important.

Figure 3 demonstrates that while the LS and STL models give rise to almost identical force profiles, the PW model results in significantly larger force drops, and a lower overall interfacial resistance. This suggests, and will be further substantiated in what follows, that while the total energy dissipated during these drops is similar in the LS and STL models, the energy dissipated in the PW model is significantly larger. Other features of the global friction curves shown in Fig. 3, such as the

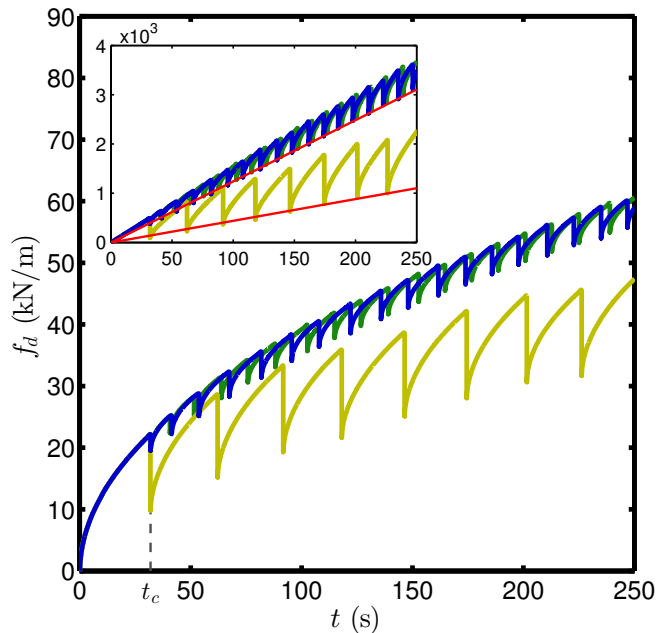


FIG. 3. The loading force f_d vs. time for the three models (color code as in Fig. 1). It is seen that all of the curves coincide for short times, and then begin to diverge. The LS and STL models maintain the same “envelope”, while the PW model features more pronounced stress drops, larger inter-event time and a lower overall resistance. (inset) The same data as in the main panel, but this time f_d^2 is plotted vs. time. The red lines are linear fits to the values of f_d^2 at the rupture arrest times t_a (i.e. f_d^2 right after the force drops), cf. the prediction in Eq. (17).

lower envelope of $f_d(t)$ (corresponding to the values of $f_d(t)$ after each drop), will be discussed and explained theoretically below.

B. Spatiotemporal interfacial dynamics

In order to understand the origin of these differences, one must examine the complex spatiotemporal dynamics that give rise to the “force drop events”, which are described at length in [23]. As stated above, the instabilities result in the nucleation, propagation and arrest of rupture fronts, a scenario reported by many experimental, numerical and analytical works [27, 41–45]. Most of the remainder of this paper will be focused on the first event, which is marked in Fig. 3 by t_c . The rationale for focussing on the first event (rather than some later event) is that it ensures that the state of the interface is the same for all three model variants at the onset of instability (with no history effects), cleanly isolating the effects of the existence and form of the velocity-strengthening branch. Having said that, we note that it is clear from Fig. 3 that the differences between the three variants persist to *any* event. Furthermore, multiple-event properties will be explicitly discussed in relation to Eqs. (15)-(17)

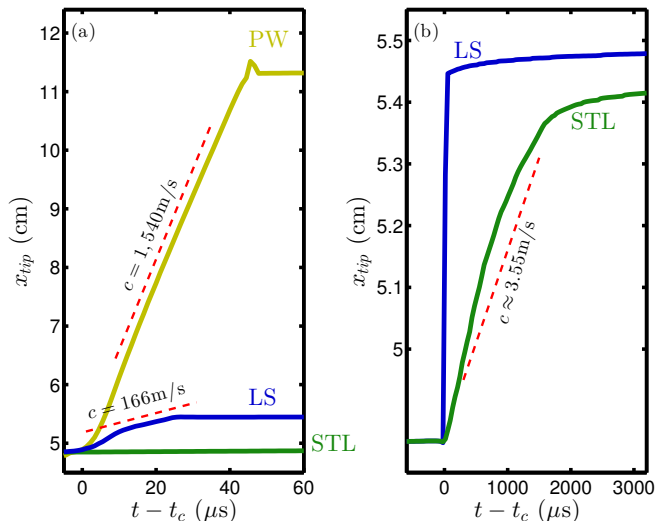


FIG. 4. Propagation of rupture fronts in the first event for (a) All three models and (b) the LS and LTS models. x_{tip} is the spatial location of the front tip, cf. Fig. 5. t_c is the time where the front starts to propagate, cf. Fig. 3. Note also the vast difference in timescales between the panels. The wave speed in this system is $\sqrt{G/\rho} \approx 2700$ m/s.

and the inset of Fig. 3.

Figure 4 shows the propagation and arrest of rupture fronts during the first event. First, we note the vast difference in the timescales involved: while rupture fronts in the LS and PW models arrest after a few $10\mu\text{s}$, in the STL model they last for a few ms. It is observed, however, that while the penetration depth of the front into the interface in the LS and STL models is comparable, for the PW model it is an order of magnitude larger. Furthermore, the rupture propagation velocity in the LS model is an order of magnitude smaller than in the PW model (the latter is of the order of the elastic wave-speed), and the propagation velocity in the STL model is yet two orders of magnitude smaller.

Both the LS and STL models give rise to rupture fronts that are much slower than the elastic wave-speed. These remarkably low rupture propagation velocities, three orders of magnitude slower than the elastic wave-speed in the STL model, might be related to the important, and rather intensely debated, issue of slow rupture [22, 46–49]. Our calculations suggest that the emergence of slow rupture might be directly related to the existence and form of velocity-strengthening friction. This is in accord with recent laboratory experiments on fault-zone materials, which documented slow slip events together with a clear crossover from velocity-weakening to velocity-strengthening friction with increasing slip velocity [12].

A lot can be learned from the state of the interface after the rupture front has passed. In Fig. 5 we plot the spatial distribution of the (normalized) friction stress just before the first rupture event and immediately after it for the three variant models. In both of these states,

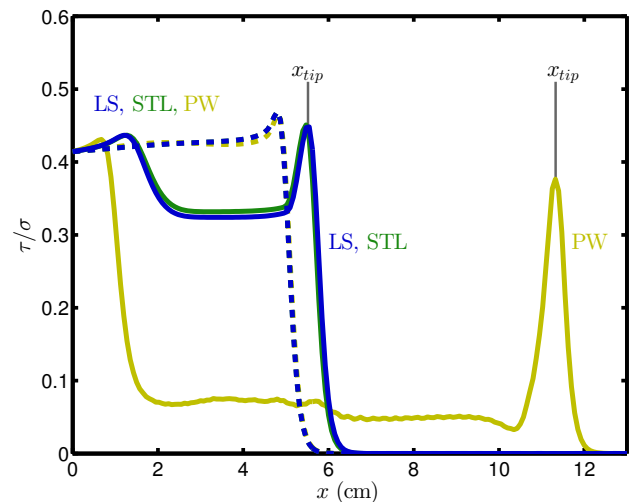


FIG. 5. The frictional stress 1s prior to the first event (dashed lines) and 1s after (solid lines). The color code is as in Fig. 1. It is seen that the stress left at the tail of the rupture fronts, τ_r , is roughly homogeneous in space, and that it is much lower in the PW model than in the LS and STL models. The location of the fronts after the event is marked by x_{tip} . The deeper penetration of the PW model, also shown in Fig. 4, is clearly visible.

the higher slip rates associated with the rupture fronts are not present (before the event they have not yet been generated and after the event they have died off), and the mechanical state is quasi-static. In line with the previous results, prior to the inception of the first event the stress profiles in the three models essentially coincide. When the fronts propagate and eventually arrest, they leave behind them a residual stress profile, which is much smaller in the PW model compared to the LS and STL models. This residual stress is approximately homogeneous in space and is lower than the stress prior to the event. The elastic energy release during this stress relaxation process is the driving force to frictional dissipation.

The approximate spatial homogeneity of τ left behind *any* rupture front when it arrests, allows us to estimate the loading force $f_d(t_a) = \int_0^L \tau(x, t_a) dx$ at the discrete arrest times t_a (that is, there is t_a corresponding to each rupture event). For that aim, we neglect the contribution to the integral in the region $x > x_{tip}(t_a)$, where $x_{tip}(t_a)$ is the location of the peak of τ slightly after a rupture front arrested (cf. Fig. 5), and then assume that $\tau(x, t_a)$ can be replaced by a constant residual stress τ_r , obtaining

$$f_d(t_a) = \int_0^L \tau(x, t_a) dx \simeq \int_0^{x_{tip}(t_a)} \tau(x, t_a) dx \simeq \tau_r x_{tip}(t_a). \quad (15)$$

To calculate $x_{tip}(t_a)$, we note that at the arrest times t_a Eq. (11) takes the form $\tau_r \simeq \bar{G}H \partial_{xx} u(x, t_a)$ (i.e. in the range $0 < x < x_{tip}(t_a)$ and neglecting inertia). With the approximate boundary conditions $u(x_{tip}) \simeq \partial_x u(x_{tip}) \simeq 0$,

this equation can be readily solved as

$$x_{tip}(t_a) \simeq \sqrt{\frac{2\bar{G}H u(x=0, t_a)}{\tau_r}}. \quad (16)$$

This can be substituted in Eq. (15) to give

$$f_d(t_a)^2 \simeq 2\bar{G}H\tau_r v_d t_a, \quad (17)$$

where $u(x=0, t_a) = v_d t_a$ was used (which is, of course, valid at any time, not only at the discrete arrest times $t = t_a$).

The prediction in Eq. (17), i.e. $f_d(t_a)^2 \sim t_a$, is tested in the inset of Fig. 3 for all three models over many events (i.e. this is a multiple-event property, not only a property of the first event, which was the focus of the discussion up to now). The analytic prediction is observed to be in favorable agreement with the numerical data for all three models, where the prefactor (slope) in the relation $f_d(t_a)^2 \sim t_a$ is the same for the LS and STL models, but is significantly smaller for the PW model. These results show that τ_r is the same for every rupture event and lend direct support to the assumption that spatial variations of the residual stress left behind *any* rupture front can be neglected, consistent with the explicit stress profiles shown in Fig. 5 (for the first event in the three different models).

The latter observation allows us to extract τ_r , the only unknown quantity in Eq. (17) (all other quantities are known parameters, which are the same for all three models), yielding $\tau_r/\sigma \simeq 0.332$ for the LS and STL models and $\tau_r/\sigma \simeq 0.122$ for the PW model. The fact that the models that feature a nonmonotonic velocity dependence, i.e. the LS and STL models, give rise to an essentially identical residual stress τ_r is intimately related to the value of the steady state stress at the minimum of the friction curve (cf. Fig. 1), which is the same for both. Equation (17) then shows that the fact that the PW model produces a lower overall frictional resistance (and deeper force drops) compared to the LS and STL models is intimately related to the fact that the residual stress left behind the rupture fronts in the PW model is significantly lower than that of the LS and STL models. Furthermore, Eq. (16) suggests an explanation for why the penetration depth, i.e. $x_{tip}(t_a)$, is significantly larger in the PW model than in the other two models.

The ‘‘static friction coefficient’’ μ_{static} is ordinarily defined as the tangential force, normalized by the normal force, needed to initiate global motion of the block. This force also corresponds to the peak of the loading curve. From this perspective, all of the spatiotemporal dynamics discussed up to now are precursory [27, 42, 43], as they precede global motion which sets in only when a rupture front reaches the leading edge of the block (i.e. when $x_{tip} = L$). Hence, we can estimate μ_{static} , which quantifies the global frictional resistance, as

$$\mu_{static} \simeq \frac{f_d(x_{tip} \simeq L)}{\sigma L} \simeq \frac{\tau_r}{\sigma}, \quad (18)$$

where Eq. (15) was used. This shows that the ‘‘static’’ frictional resistance of the interface, measured at slow loading velocities (here $v_d = 10\mu\text{m/s}$), is influenced by dynamic processes at much higher slip rates and furthermore that the existence of velocity-strengthening friction behavior strongly affects μ_{static} through τ_r [40, 50, 51].

The results discussed above highlight two important points. First, an effectively constant residual stress τ_r is left behind rupture fronts in all of the models studied here. This property emerges spontaneously, unlike conventional slip-weakening models in which it is assumed a priori (see, for example, [41, 44, 52] and the discussion in [53]). The value of τ_r depends on the existence of velocity-strengthening friction, which in turn has significant implications on the strength of the interface, as evident from Fig. 3 and Eq. (18). Note also that the constancy of the residual stress τ_r implies that the mechanical fields associated with frictional shear cracks in 2D are well described by the classical theory of fracture [54]. Second, once τ_r is known, the arrest of rupture fronts is determined by global equilibrium conditions [55], rather than by dynamic considerations (cf. Eq. (15)).

C. Energy partition: Dissipation and radiation

As energy dissipation is at the heart of frictional phenomena, it will be interesting and instructive to consider the energy budget in the system. As a starting point, we briefly remind the reader that the linear momentum conservation law of Eq. (10) can be transformed into a continuity equation for the energy density (using Hooke’s law and integration by parts). The result reads

$$\partial_t \left(\frac{1}{2}\rho (\partial_t u_i)^2 + \frac{1}{2}\epsilon_{ij}\sigma_{ij} \right) - \partial_j \left(\sigma_{ij}\partial_t u_i \right) = 0. \quad (19)$$

The first term is the rate of variation of the energy density (both kinetic and elastic), and the second term is the divergence of the energy flux vector. Their sum vanishes when energy is conserved.

Following the same procedure, one can derive the energy continuity equation for our model by combining Eqs. (5) and (11), obtaining

$$\partial_t (\epsilon_k + \epsilon_c + \epsilon_i) - \partial_x J = -p_i - p_{vis} \equiv -p, \quad (20)$$

where we defined

$$\begin{aligned} \epsilon_k &\equiv \frac{1}{2}\rho H (\partial_t u)^2, & \epsilon_c &\equiv \frac{1}{2}\bar{G}H (\partial_x u)^2, \\ \epsilon_i &\equiv \frac{(\tau^{el})^2}{2G_0 A/h}, & J &\equiv \bar{G}H v \partial_x u, \\ p_i &\equiv 2\epsilon_i \frac{|v|}{D}, & p_{vis} &\equiv \tau^{vis} v. \end{aligned} \quad (21)$$

Here ϵ_k is the kinetic energy density, ϵ_c is the (bulk) linear elastic strain energy density, ϵ_i is the interfacial elastic energy density and J is the energy flux. The interfacial energy density, ϵ_i , is dissipated during sliding

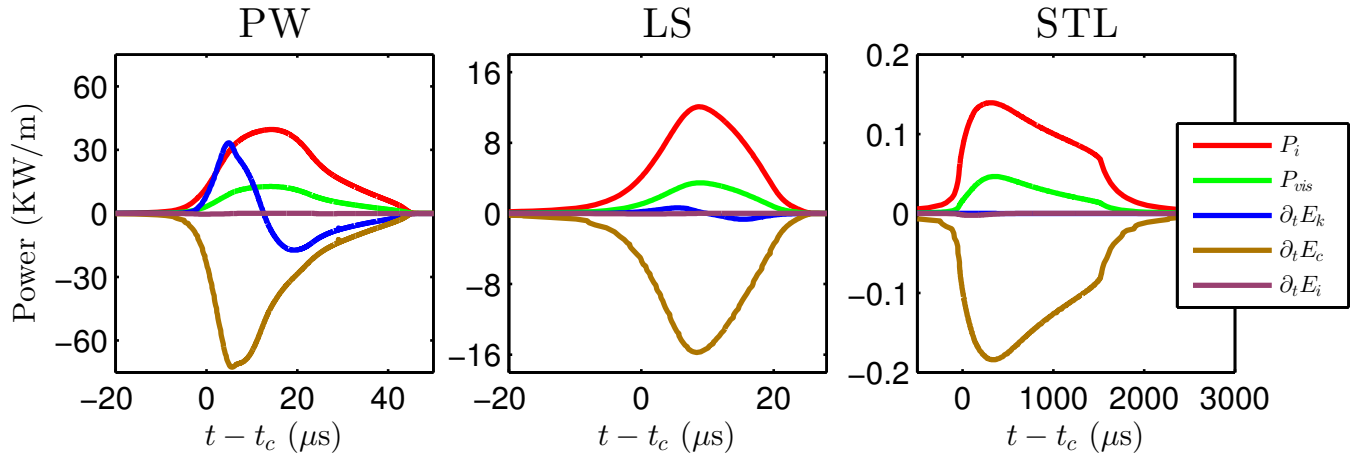


FIG. 6. The rate of change of energies $\partial_t E_\gamma(t) = \partial_t \int_0^L \varepsilon_\gamma(x, t) dx$ and dissipation rates $P_\gamma(t) = \int_0^L p_\gamma(x, t) dx$ ($\varepsilon_\gamma(x, t)$ and $p_\gamma(x, t)$ are defined in Eqs. (21)) during the first event for the three models.

due to the rupture of asperities, resulting in a dissipation rate p_i [56], in addition to the standard dissipation rate $p_{vis} = \tau^{vis} v$.

Equation (20) has the same structure as Eq. (19), except for the non-vanishing dissipation rate p , which exists because frictional dynamics are dissipative, and the existence of an interfacial elastic contribution ε_i (both in the stored energy and in the dissipation power p_i).

The quantities defined in Eq. (21) are densities that exhibit complex spatiotemporal behaviors during frictional instabilities (which result in rupture events). In order to gain some insight into these complex energy-exchange processes, it will be useful to consider the corresponding space-integrated quantities $E_\gamma(t) = \int_0^L \varepsilon_\gamma(x, t) dx$ and $P_\gamma(t) = \int_0^L p_\gamma(x, t) dx$.

The interplay between these various quantities during frictional instabilities (“events”), shown for all three models in Fig. 6, is an essential feature of interfacial dynamics. Our goal is to quantify generic energy-exchange processes during frictional instabilities [57] and in particular to understand the differences between the three models in this respect. As the dynamics during frictional instabilities are much faster than typical loading rates, we expect them to be exclusively driven by the already stored elastic energy. That is, we expect the rate of change of the sum of bulk and interfacial elastic energies, $\partial_t(E_c + E_i)$, to be negative during an event. Figure 6 clearly demonstrates this, and that $\partial_t E_i$ is negligible compared to $\partial_t E_c$ (hence we neglect the former compared to the latter in what follows).

The time integral of $\partial_t E_c$ over the event duration is the total energy released, which is a natural measure of the magnitude of the event (other measures exist as well). The elastic energy released is either being dissipated directly or is being first transformed into kinetic energy (“radiation”). Eventually, the kinetic energy is also dissipated. This generic picture is demonstrated in Fig. 6 for all three models. In particular, it is observed that

the dissipation contributions P_i and P_{vis} are comparable, where the former is typically larger than the latter. Kinetic energy generation (“radiation”), $\partial_t E_k > 0$, is observed in the first part of the event. In the second part of the event $\partial_t E_k < 0$, when the kinetic energy decays and is being dissipated.

While this generic qualitative picture is similar in all three models, there are large quantitative differences that we wish to discuss now. The main characteristics of the first rupture event in the LS, STL and PW models are summarized in Table II. As we already know from Fig. 4, the events are mediated by rupture fronts of vastly different velocities in the three models ($\sim 10^3$ m/s in the PW model, $\sim 10^2$ m/s in the LS model and ~ 1 m/s in the STL model). The event duration is about 40% larger in the PW model as compared to the LS model, both in the few $10 \mu\text{s}$ range, while it is two orders of magnitude larger in the STL model ($\sim \text{ms}$). Despite the vast differences in the rupture propagation velocity and event duration, the total dissipated energy (which equals the amount of elastic energy released during the event) in the LS and STL models is essentially identical. This is in line with Fig. 3, which shows that the two models feature nearly identical stress drops and frictional resistance, and with Fig. 5 and the inset of Fig. 3, which show that the residual stress τ_r in the two models is essentially identical. This result clearly demonstrates that depending on the form of the velocity-strengthening friction branch (e.g. logarithmic vs. linear) one can observe events of the same magnitude (i.e. integrated dissipation/energy release) accompanied by very different dissipation rates (see Table II). This result might be related to geophysical observations indicating that slow rupture does not necessarily imply smaller integrated slip and energy release [46, especially Figure 5].

The total dissipation in the PW model is about 5.4 times larger than the total dissipation in the LS and STL models, consistent with the much larger stress drops and

	PW	LS	STL
Velocity strengthening	Absent	Logarithmic	Linear
Rupture propagation speed	1540 m/s	166 m/s	~ 3 m/s
Event's duration Δt	$\sim 50 \mu s$	$\sim 35 \mu s$	$\sim 2000 \mu s$
Total dissipated energy ^a	1.4 J/m	0.26 J/m	0.26 J/m
Maximal dissipation rate ^b	52 kW/m	16 kW/m	0.19 kW/m
Total radiated energy ^c	0.27 J/m	4.5 mJ/m	0.54 μ J/m
Penetration length $x_{tip}(t_a)$	11.3 cm	5.52 cm	5.46 cm

^a Approximately equals to the bulk elastic energy released during the event, $\int_{\Delta t} \partial_t E_c dt$.

^b The maximum of $P = P_i + P_{vis}$.

^c The maximum of E_k .

TABLE II. Summary of the main characteristics of the first rupture event in the LS, STL and PW models.

the significantly reduced interfacial resistance observed in Fig. 3. Moreover, the amount of kinetic energy generated during the event is much larger in the PW model as compared to the other two models, and is about 19% of the total energy released (though eventually it is also dissipated). In systems of larger heights H , this radiated kinetic energy will decay on longer timescales, allowing it to interact with remote boundaries. The kinetic energy generated in the STL model is negligibly small, while in the LS it makes about 1.7% of the released energy (a similar value was reported in [57], although direct comparison is precarious). All in all, these results provide strong evidence that the existence and form of velocity-strengthening friction has significant implications on frictional dynamics and strength.

IV. CONCLUSIONS

In conclusion, by studying the spatiotemporal dynamics in three variants of a realistic rate-and-state friction model under quasi-static side-loading conditions, we showed that the existence and form of velocity-strengthening friction may significantly affect various aspects of the frictional response of interfaces. These in-

clude the propagation velocity of coherent fronts that mediate interfacial rupture events, the emergence of slow rupture, the elastic energy released during events (i.e. their magnitude), the dissipation and radiation rates, and the global frictional resistance (strength). The clear connection between the existence of velocity-strengthening friction and slow rupture appears to be directly related to the recent experimental results of [12]. It is also shown that events of similar magnitude (and hence stress drops) can be accompanied by substantially different dissipation and kinetic energy radiation rates.

Our theoretical results, together with extensive experimental evidence [16], highlight the need to quantitatively characterize the velocity-strengthening frictional response of interfaces, both experimentally and theoretically, and to systematically incorporate it into friction theory. Since frictional instabilities spontaneously lead to accelerated slip that probes relatively high-velocity properties of frictional interfaces, the latter – which include velocity-strengthening friction – affect the frictional response even under quasi-static loading conditions. This understanding may offer new ways to interpret existing observations in a broad range of frictional systems and to develop predictive theories of the dynamics of spatially extended frictional interfaces.

-
- [1] J. H. Dieterich, *Pure Appl. Geophys.* **116**, 790 (1978).
 - [2] A. Ruina, *J. Geophys. Res.* **88**, 10359 (1983).
 - [3] C. J. Marone, *Annu. Rev. Earth Planet. Sci.* **26**, 643 (1998).
 - [4] B. N. J. Persson, *Sliding friction: physical principles and applications* (Springer-Verlag, Berlin, 2000).
 - [5] C. H. Scholz, *The Mechanics of Earthquakes and Faulting* (Cambridge University Press, Cambridge, 2002).
 - [6] T. Baumberger and C. Caroli, *Adv. Phys.* **55**, 279 (2006).
 - [7] J. R. Rice and A. Ruina, *J. Appl. Mech.* **50**, 343 (1983).
 - [8] J.-C. Gu, J. R. Rice, A. Ruina, and S. T. Tse, *J. Mech. Phys. Solids* **32**, 167 (1984).
 - [9] F. Heslot, T. Baumberger, B. Perrin, B. Caroli, and C. Caroli, *Phys. Rev. E* **49**, 4973 (1994).
 - [10] T. Baumberger and P. Berthoud, *Phys. Rev. B* **60**, 3928 (1999).
 - [11] J. R. Rice, N. Lapusta, and K. Ranjith, *J. Mech. Phys. Solids* **49**, 1865 (2001).
 - [12] B. M. Knap and C. J. Marone, *Science* **341**, 1229 (2013).
 - [13] C. J. Marone, C. B. Raleigh, and C. H. Scholz, *J. Geophys. Res.* **95**, 7007 (1990).
 - [14] A. M. Rubin and J.-P. Ampuero, *J. Geophys. Res.* **110**, B11312 (2005).
 - [15] Y. Liu, *J. Geophys. Res.* **110**, B08307 (2005).
 - [16] Y. Bar-Sinai, R. Spatschek, E. A. Brener, and E. Bouchbinder, *J. Geophys. Res. Solid Earth* **119**, 1738 (2014).
 - [17] J. D. Weeks, *J. Geophys. Res.* **98**, 17637 (1993).
 - [18] N. Kato, *Earth Planet. Sci. Lett.* **216**, 17 (2003).
 - [19] B. Shibazaki and Y. Iio, *Geophys. Res. Lett.* **30**, 1489 (2003).
 - [20] E. Bouchbinder, E. A. Brener, I. Barel, and M. Urbakh,

- Phys. Rev. Lett. **107**, 235501 (2011).
- [21] Y. Bar-Sinai, E. A. Brener, and E. Bouchbinder, Geophys. Res. Lett. **39**, L03308 (2012).
- [22] J. C. Hawthorne and A. M. Rubin, J. Geophys. Res. Solid Earth **118**, 1216 (2013).
- [23] Y. Bar-Sinai, R. Spatschek, E. A. Brener, and E. Bouchbinder, Phys. Rev. E **88**, 060403(R) (2013).
- [24] C. J. Marone, C. H. Scholz, and R. Bilham, J. Geophys. Res. **96**, 8441 (1991).
- [25] E. A. Brener and V. I. Marchenko, JETP Lett. **76**, 211 (2002).
- [26] E. A. Brener, S. V. Malinin, and V. I. Marchenko, Eur. Phys. J. E **17**, 101 (2005).
- [27] O. M. Braun, I. Barel, and M. Urbakh, Phys. Rev. Lett. **103**, 194301 (2009).
- [28] M. Nakatani and C. H. Scholz, J. Geophys. Res. **111**, B12208 (2006).
- [29] O. Ben-David, S. M. Rubinstein, and J. Fineberg, Nature **463**, 76 (2010).
- [30] T. Putelat, J. H. Dawes, and J. R. Willis, J. Mech. Phys. Solids **59**, 1062 (2011).
- [31] T. E. Tullis and J. D. Weeks, Pure Appl. Geophys. **124**, 383 (1986).
- [32] K. Nagata, M. Nakatani, and S. Yoshida, Geophys. Res. Lett. **35**, L06310 (2008).
- [33] M. Nakatani, J. Geophys. Res. **106**, 13347 (2001).
- [34] J.-P. Ampuero and A. M. Rubin, J. Geophys. Res. **113**, B01302 (2008).
- [35] S. Rubinstein, G. Cohen, and J. Fineberg, Phys. Rev. Lett. **98**, 226103 (2007).
- [36] O. Ben-David, G. Cohen, and J. Fineberg, Tribol. Lett. **39**, 235 (2010).
- [37] P. Berthoud and T. Baumberger, Europhys. Lett. **41**, 617 (1998).
- [38] L. Bureau, C. Caroli, and T. Baumberger, Proc. R. Soc. A Math. Phys. Eng. Sci. **459**, 2787 (2003).
- [39] J. Trømborg, J. Scheibert, D. S. Amundsen, K. Thøgersen, and A. Malthé-Sørenssen, Phys. Rev. Lett. **107**, 074301 (2011).
- [40] M. Otsuki and H. Matsukawa, Sci. Rep. **3**, 1586 (2013).
- [41] M. Ohnaka, Pure Appl. Geophys. **157**, 2259 (2000).
- [42] S. M. Rubinstein, G. Cohen, and J. Fineberg, Nature **430**, 1005 (2004).
- [43] O. Ben-David, G. Cohen, and J. Fineberg, Science **330**, 211 (2010).
- [44] D. S. Kammer, V. A. Yastrebov, P. Spijker, and J.-F. Molinari, Tribol. Lett. **48**, 27 (2012).
- [45] S. Latour, A. Schubnel, S. Nielsen, R. Madariaga, and S. Vinciguerra, Geophys. Res. Lett. **40**, (2013).
- [46] Z. Peng and J. Gomberg, Nat. Geosci. **3**, 599 (2010).
- [47] A. Kato, K. Obara, T. Igarashi, H. Tsuruoka, S. Nakagawa, and N. Hirata, Science **335**, 705 (2012).
- [48] M. J. Ikari, C. J. Marone, D. M. Saffer, and A. J. Kopf, Nat. Geosci. **6**, 468 (2013).
- [49] J. Trømborg, H. A. Sveinsson, J. Scheibert, K. Thøgersen, D. S. Amundsen, and A. Malthé-Sørenssen, Proc. Nat. Acad. Sci. U.S.A **111**, 8764 (2014).
- [50] O. Ben-David and J. Fineberg, Phys. Rev. Lett. **106**, 254301 (2011).
- [51] R. Capozza and M. Urbakh, Phys. Rev. B **86**, 085430 (2012).
- [52] K. Uenishi and J. R. Rice, J. Geophys. Res. **108**, 2042 (2003).
- [53] M. Cocco and A. Bizzarri, Geophys. Res. Lett. (2002).
- [54] I. Svetlizky and J. Fineberg, Nature **509**, 205 (2014).
- [55] A. Taloni, A. Benassi, S. Sandfeld, and S. Zapperi, unpublished.
- [56] p_i , defined in Eq. (21), in fact contains also a contribution of the form $\varepsilon_i \dot{A}/A$. As this contribution is negligibly small in our calculations, we omitted it.
- [57] Z. Shi, Y. Ben-Zion, and A. Needleman, J. Mech. Phys. Solids **56**, 5 (2008).